OVERVIEW OF NEW MAST PHYSICS IN ANTICIPATION OF FIRST RESULTS FROM MAST UPGRADE

J. R. Harrison[1], RJ Akers[1], SY Allan[1], JS Allcock[1,2], JO Allen[3], L Appel[1], M Barnes[1,4,5], N Ben Ayed[1], W Boeglin[6], C Bowman[3], J Bradley[7], P Browning[8], P Bryant[7], M Carr[1], M Cecconello[9], CD Challis[1], S Chapman[10], IT Chapman[1], GJ Colyer[4,11], S Conroy[9], NJ Conway[1], M Cox[1], G Cunningham[1], RO Dendy[1,10], W Dorland[4,19], BD Dudson[3], L Easy[1,3], SD Elmore[1], T Farley[1,7], X Feng[2], AR Field[1], A Fil[3], GM Fishpool[1], M Fitzgerald[1], K Flesch[12], MFJ Fox[1,4,13], H Frerichs[12], S Gadgil[10], D Gahle[1,14], L Garzotti[1], Y-C Ghim[1,4,20], S Gibson[1,2], KJ Gibson[3], S Hall[1], C Ham[1], N Heiberg[1], SS Henderson[1], E Highcock[4,21], B Hnat[10], J Howard[15], J Huang[22], SWA Irvine[10], AS Jacobsen[23], O Jones[1,2], I Katramados[1], D Keeling[1], A Kirk[1], I Klimek[9], L Kogan[1], J Leland[1,7], B Lloyd[1], J Lovell[16], B Madsen[17], O Marshall[3], R Martin[1], G McArdle[1], K McClements[1], B McMillan[10], A Meakins[1], HF Meyer[1], F Militello[1], J Milnes[1], S. Mordijck[24], AW Morris[1], D Moulton[1], D Muir[1], K Mukhi[1,8], S Murphy-Sugrue[1,7], O. Myatra[3], G Naylor[1], P Naylor[3], SL Newton[1], T O'Gorman[1], J Omotani[1], MG O'Mullane[14], S Orchard[1,3], SJP Pamela[1], L Pangione[1], F Parra[1,4], RV Perez[6], L Piron[1], M Price[1], ML Reinke[16], F Riva[1], CM Roach[1], D Robb[25], D Ryan[1], S Saarelma[1], M Salewski[17], S Scannell[1], AA Schekochihin[4,13], O Schmitz[12], S Sharapov[1], R Sharples[2], SA Silburn[1], SF Smith[1,3], A Sperduti[9], R Stephen[1], NT Thomas-Davies[1], AJ Thornton[1], M Turnyanskiy[1], M Valovič[1], F Van Wyk[1,4,18], RGL Vann[3], NR Walkden[1], I Waters[12], HR Wilson[1,3] and the MAST-U Team and the EUROfusion MST1 team[*]

Email: James.Harrison@ukaea.uk

[1] CCFE, Culham Science Centre, Abingdon, Oxon, OX14 3DB, United Kingdom
[2] Centre for Advanced Instrumentation, Durham University, South Road, Durham, DH1 3LE, UK
[3] York Plasma Institute, Department of Physics, University of York, Heslington, York YO10 5DD, United Kingdom
[4] Rudolf Peierls Centre for Theoretical Physics, University of Oxford, OX1 3NP, United Kingdom
[5] Plasma Science and Fusion Center, 167 Albany Street, Cambridge, MA 02139, United States of America
[6] Department of Physics, Florida International University, 11200 SW, Miami, FL 33199, USA
[7] Department of Electrical Engineering and Electronics, University of Liverpool, Brownlow Hill, Liverpool L69 3GJ, United Kingdom
[8] School of Physics and Astronomy, University of Manchester, Oxford Road, Manchester M13 9PL, United Kingdom
[9] Department of Physics and Astronomy, Uppsala University, SE-751 05 Uppsala, Sweden
[10] Centre for Fusion, Space and Astrophysics, Department of Physics, University of Warwick, Coventry, CV4 7AL, United Kingdom
[11] Engineering, Mathematics and Physical Sciences, University of Exeter, EX4 4QF, United Kingdom
[12] University of Wisconsin-Madison, Madison, Wisconsin, USA
[13] Merton College, Oxford, OX1 4JD, United Kingdom
[14] Department of Physics SUPA, University of Strathclyde, Glasgow, G4 ONG, UK
[15] Plasma Research Laboratory, Australian National University, Canberra, ACT 0200, Australia
[16] Oak Ridge National Laboratory, Oak Ridge, TN 37831, USA
[17] Department of Physics, Technical University of Denmark, Kgs. Lyngby, Denmark
[18] STFC Daresbury Laboratory, Daresbury, Cheshire, WA4 4AD, United Kingdom
[19] Department of Physics, University of Maryland, College Park, MD 20742-4111, United States of America
[20] Department of Nuclear and Quantum Engineering, KAIST, Daejeon, 34141, Republic of Korea
[21] Chalmers University of Technology, Department of Physics, Göteborg SE-412 96, Sweden
[22] Institute of Plasma Physics, Chinese Academy of Sciences, P.O. 1126, 230031 Hefei, Anhui, China
[23] Max-Planck-Institut für Plasmaphysik, Garching, Germany
[24] Dept. of Computer Science, College of William & Mary, Williamsburg, VA, US
[25] Department of Physics and Astronomy, University of Glasgow, Glasgow G12 8QQ, United Kingdom

Abstract

The Mega Amp Spherical Tokamak (MAST) was a low aspect ratio device (R/A = 0.85/0.65 ~ 1.3) with similar poloidal cross-section to other medium-size tokamaks. The physics programme concentrates on addressing key physics

_____

[*] See the author list of "H. Meyer et al 2017 Nucl. Fusion 57 102014"

issues for the operation of ITER, design of DEMO and future spherical tokamaks through utilising highly resolved diagnostic measurements closely coupled with theory and modelling to make significant advances in our understanding. An empirical scaling of the energy confinement time that favours higher power, lower collisionality devices is consistent with gyrokinetic modelling of electron scale turbulence. Measurements of ion scale turbulence with beam emission spectroscopy and gyrokinetic modelling in up-down symmetric plasmas find that the symmetry is broken in the presence of flow shear. Near the non-linear stability threshold, this leads to tilted density fluctuation correlation functions and skewed fluctuation distribution functions. Sawteeth are found to redistribute passing and trapped fast particles injected from neutral beam injectors in equal measure, suggesting that resonances between the $m=1$ perturbation and the fast ion orbits may be playing a dominant role in the fast ion transport. Measured D-D fusion products from a neutron camera and a charged fusion product detector are 40% lower than predictions from TRANSP/NUBEAM, highlighting possible deficiencies in the guiding centre approximation. Modelling of fast ion losses in the presence of resonant magnetic perturbations (RMPs) can reproduce trends observed in experiments when the plasma response and charge-exchange losses are accounted for. Measurements with a neutral particle analyser during merging-compression start-up indicate the acceleration of ions and electrons. Reciprocating probe measurements have characterised a geodesic acoustic mode at the edge of an ohmic L-mode plasma and particle-in-cell modelling has improved the interpretation of plasma potential estimates from ball-pen probes. The application of RMPs leads to a reduction in particle confinement in L-mode and H-mode and an increase in the core ionization source. The ejection of secondary filaments following type-I ELMs correlates with interactions with surfaces near the X-point. Simulations of the interaction between pairs of filaments in the scrape-off layer suggest this results in modest changes to their velocity, and in most cases can be treated as moving independently. A stochastic model of scrape-off layer profile formation based on the superposition of non-interacting filaments is in good agreement with measured time-average profiles. Fast camera imaging of the divertor indicate the presence of a quiescent region devoid of filament near the X-point, extending from the separatrix to $\psi_n \sim 1.02$. Simulations of turbulent transport in the divertor show that the angle between the divertor leg on the curvature vector strongly influences transport into the private flux region via the interchange mechanism. Coherence imaging measurements show counter-streaming flows of impurities due to gas puffing increasing the pressure on field lines where the gas is ionised. MAST Upgrade is based on the original MAST device, with substantially improved capabilities to operate with a Super-X divertor to test extended divertor leg concepts. SOLPS-ITER modelling predicts the detachment threshold will be reduced by more than a factor of 2, in terms of upstream density, in the Super-X compared with a conventional configuration and that the radiation front movement is passively stabilised before it reaches the X-point. 1D fluid modelling reveals the key role of atomic physics in governing detachment onset and evolution. Analytic modelling indicates that long legs placed at large major radius, or equivalently low $|B|$ at the target compared with the X-point are more amenable to external control. With MAST Upgrade experiments expected in 2019, a thorough characterisation of the sources of the intrinsic error field has been carried out and a mitigation strategy developed.

1. INTRODUCTION

MAST Upgrade is a low aspect ratio device ($R/a = 0.85/0.65 \sim 1.3$) based on the MAST tokamak that will start operating in 2019 with substantially improved capabilities, including 17 new poloidal field coils (14 of which are within the vacuum vessel), new closed, up-down symmetric divertors with Super-X capability fitted with cryopumps, 50% higher toroidal field (from 0.585T to 0.92T at R=0.7m) and a new solenoid will nearly double the inductive flux from 0.9Vs to 1.7Vs, allowing for the maximum plasma current and pulse length to be 2MA and 5s respectively, although not concurrently, (from 1.35MA and 0.7s) and a combination of on and off-axis neutral beam heating and current drive. The physics a programme has a strong emphasis on utilising its unique divertor and core capabilities to address key issues for the success of ITER operations and the design of future devices [1], including exploring reactor-relevant alternative divertor configurations, adding to the knowledge base for ITER and to explore the performance of spherical tokamaks at higher magnetic field, shaping and auxiliary heating.

Results from analysis of MAST data and numerical modelling are presented where there is a unique contribution to predicting the performance of future devices, in particular MAST Upgrade (MAST-U). Starting from the centre of the plasma in the core, MAST data and gyrokinetic modelling of ion scale turbulence and simulations of electron scale turbulence are discussed in section 2. In section 3, fast particle physics studies of the impact of sawteeth and Resonant Magnetic Perturbations (RMPs) on fast ion confinement, characterisation of a neutron deficit and evidence for the acceleration of electrons and ions during merging-compression start-up on MAST are discussed. In section 4, new insights into transport at the edge of the confined plasma using a reciprocating probe are presented, including measurements of a Geodesic Acoustic Mode, the impact of RMPs on particle confinement, measurements of secondary ELM filaments in MAST and initial modelling of ELMs in MAST-U with JOREK are presented. In section 5, measurements and modelling of transport in the divertor and scrape-off layer are presented, together with modelling of detachment and the influence of the divertor geometry on its access and evolution. An overview of the preparations for initial operations of MAST Upgrade are

presented in section 6, with details of a package of further enhancements to address key gaps in our understanding of plasma exhaust approaching reactor relevant conditions.

2. CORE TRANSPORT & CONFINEMENT

Spherical tokamaks such as MAST are an excellent environment for studying core transport in very challenging conditions with high β, flows (and flow shear) and fast ion pressure. Previous experiments on MAST and NSTX find that the energy confinement time varied according to the scaling $B\tau_E \propto v_*^{-0.82\pm0.1}$ [2, 3], where B is the magnetic field, τ_E is the energy confinement time and v_* is collisionality, is favourable for higher power devices with closed divertors that can reach lower collisionality such as MAST Upgrade. This trend is consistent with electrostatic simulations of ETG scale turbulence in MAST using the gyrokinetic flux-tube code GS2 [4] run for sufficiently long (~0.01τ_E) to allow for turbulence initially dominated by radially elongated streamer-like structures to reach a long-term saturated state dominated by slowly growing zonal modes, which form the turbulence into 'vortex streets'. The collisionality dependence of the saturated heat flux in the simulations is due to collisional damping of the zonal modes.
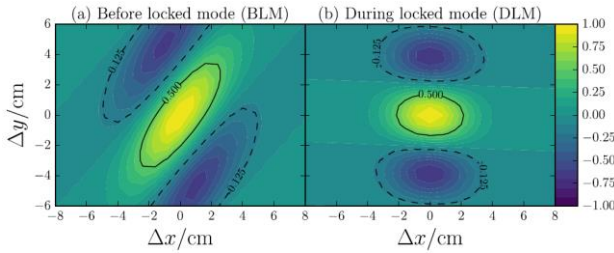

Figure 1: Spatial two-point correlation function of density fluctuations before (left) and during (right) the onset of a locked mode that reduces the toroidal flow shear. Reproduced from [Fox2017b]

Transport due to ion scale turbulence is normally strongly suppressed by flow shear which alters the characteristics of the remaining structures generated by the turbulence. Sophisticated analysis techniques have been applied to Beam Emission Spectroscopy (BES) data, taking the detector point-spread function into account [5] to derive spatial correlation parameters of density fluctuations in neutral beam heated plasmas. In up-down symmetric double null plasmas, toroidal flow shear breaks the symmetry [6]. Close to the nonlinear stability threshold, this results in a tilting of the spatial correlation function due to the shearing of turbulent structures by the mean flow where the tilt angle increases with flow shear, as shown in Figure 1. This can also result in a skewed distribution of the density fluctuations. This is not inconsistent with gyro-kinetic simulations of MAST equilibria, close to threshold, where the turbulence is dominated by a few, isolated, long-lived structures [7]. The simulations suggest that further from the threshold, the symmetry is effectively restored, reducing both the tilt of the correlation function and skewness of the distribution.
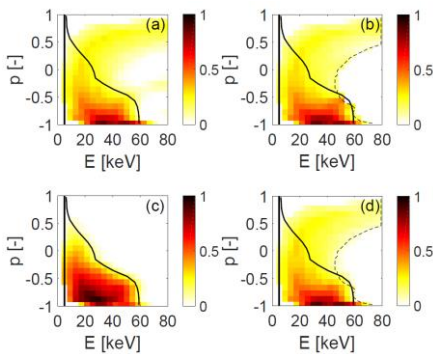
3. FAST PARTICLE PHYSICS

Figure 2: Reconstructions of the FIDASIM (a-b) and experimental (c-d) normalised fast ion distributions in pitch and energy before and after a sawtooth crash. The black curves mark a boundary outside which fast ions had only a low probability of being present, according to a neoclassical TRANSP simulation. Reproduced from [9].

In future devices where a significant proportion of the plasma heating comes from alpha-particles generated by fusion reactions, confinement of energetic particles in the presence of MHD instabilities that cause the redistribution, and sometimes loss, of energetic particles, is a significant issue. Studies of the effects of sawteeth on fast ion confinement [8], based principally on neutron camera data, indicate that passing and trapped fast particles are redistributed in equal measure. There is no evidence of an energy threshold for redistribution of passing or trapped particles due to sawteeth, suggesting that resonances between the m=1 sawtooth perturbation and the fast ion orbit (both the poloidal bounce and toroidal precession) frequencies may be playing a dominant role in the fast ion transport. A novel tomographic reconstruction

technique, based on the assumption that fast ions have only a low probability of having energies and pitches above a limit obtained from neoclassical TRANSP simulations, has been applied to fast ion deuterium-alpha (FIDA) data to reconstruct the fast particle distributions in pitch and energy space before and after a sawtooth [9]: these are in reasonable agreement with TRANSP/FIDASIM simulations, as shown in Figure 2.

Fluxes of D-D fusion products in MAST measured independently with the neutron camera and a charged fusion product detector are approximately 40% lower than those predicted by the TRANSP/NUBEAM codes [10]. An anomalous fast ion diffusivity is sometimes required to obtain a good match between TRANSP/NUBEAM and the neutron camera measurements, ranging from 0 m^2s^{-1} in quiescent scenarios to 3 m^2s^{-1} where MHD instabilities are present. A possible explanation for the discrepancy is the guiding centre approximation used in NUBEAM that leads to an over-estimate of the neutron emissivity, motivating future studies with full orbit following codes. Simulations of fast ion losses caused by resonant magnetic perturbations (RMPs), carried out using a non-steady-state orbit-following Monte-Carlo code (NSS OFMC), show that both the plasma response to the RMPs and charge-exchange reactions with background neutrals must be taken into account in order to reproduce accurately the temporal behaviour of the measured neutron rate in 400kA MAST pulses with RMPs [11].

Studies of neutral particle analyser (NPA) and microwave data have revealed that magnetic reconnection during merging-compression plasma start-up in MAST resulted in the acceleration of both ions and electrons [12]. While merging-compression will not be used as a start-up method in MAST Upgrade, it is intended that particle acceleration due to other types of reconnection event will be studied using new fast ion diagnostics, including a scintillator-based fast ion loss detector [13] and a solid state NPA.

4. EDGE, PEDESTAL AND ELMS

Understanding the transport mechanisms prevailing at the plasma edge is essential to understand and predict global confinement and L-H transitions. Detailed measurements of electrostatic potential fluctuations have yielded new observations of mode activity that can regulate the transport in this region. Measurements from an ohmic L-mode plasma indicate the presence of a Geodesic Acoustic Mode 2cm inside the separatrix, with a frequency of ~10kHz, maximum radial mode number $k_r\rho_p$ ~ -0.15 and radial phase velocity of 1km/s [14]. Estimates of the plasma potential and T_e radial profiles from ball-pen probe measurements have been improved through particle-in-cell modelling showing ions reach the recessed Langmuir probe via a combination of their Larmor orbits and ExB drifts due to electrons polarising the material leading to the probe [15], which provides a firm basis for the interpretation of plasma potential measurements [16].

The impact of RMPs applied to mitigate ELMs on neutral fuelling and exhaust have been studied using a global particle balance model in L-mode and H-mode [17]. The particle confinement time is found to reduce by ~20% in L-mode and ~30% in H-mode between ELMs relative to before the RMP was applied, where perturbations with toroidal mode numbers n=3, 4 were applied respectively. In L-mode, the application of RMPs leads to increased D_α emission at the outer mid-plane, suggesting an increase in neutral fuelling.

The characteristics of unmitigated ELMs have been studied using fast imaging data, showing that following the ejection of type-I ELMs, secondary filaments have been observed up to 1ms following the ELM, concurrent with an increase in the width of the SOL. The appearance of secondary filaments correlates
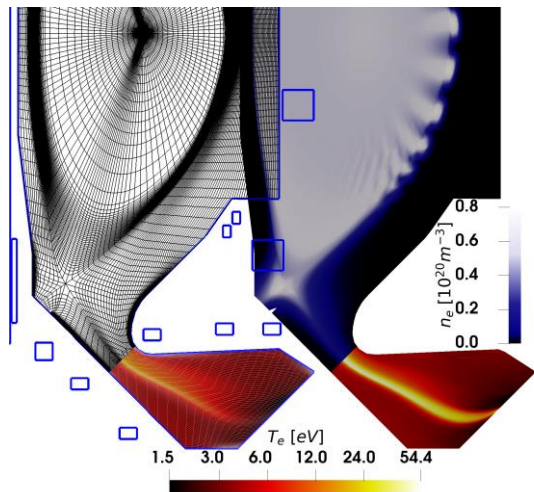

Figure 3: Predicted temperature (red) and density (blue) profiles across the MAST-U divertor chamber before (left) and after (right) the triggering of an ELM releasing a heat pulse into the divertor, simulated using JOREK.

with plasma interaction with poloidal field coils near the X-point. This will be the subject of further study in MAST-U using the baffling structures at the entrance to the closed divertors.

Initial simulations of the propagation of large type-I ELMs through a Super-X divertor configuration in MAST-U have been carried out, showing the ELM burn through the cold ($T_e < 5eV$), dense plasma in the divertor, as illustrated in Figure 3. These and future simulations will be used to guide experiments exploring whether closed divertors, long divertor legs and ELM mitigation techniques can effectively exhaust the ELM energy before it reaches the divertor targets.

5. SCRAPE-OFF LAYER AND DIVERTOR

Finding a solution to the exhaust of heat and particles is of paramount importance for the operation of ITER and design of future reactors. The concentration of heat and particle loads, which must be reduced to avoid damaging the first wall and divertor, is strongly governed by filamentary transport across the scrape-off layer (SOL) and transport along the magnetic field. Data from MAST experiments, together with detailed modelling, have yielded key insights into the nature of filamentary transport with a conventional open divertor in preparation for studies in alternative divertors such as the Super-X in MAST Upgrade.

The interaction between pairs of filaments of varying size and separation has been studied with BOUT++ simulations [18]. This interaction occurs when the dipolar electrostatic fields associated with the filaments merge or cancel each other, thereby altering the centre-of-mass velocity of the pair of filaments. The interaction quickly decays with increasing filament separation, resulting in changes in their velocity of ≤50% for filaments seeded ~1 width apart. Conversely, filaments separated by more than 5x their width are found to behave independently. This finding adds credence to stochastic models that treat the SOL density profile as the superposition of non-interacting filaments. One such model [19], that treats the production of filaments as a Poisson process and includes radial transport and draining of particles and energy along field lines has recently been extended to accommodate filaments launched from different toroidal locations with a finite toroidal velocity, with distribution functions of the filament amplitude, radial and toroidal extent, and toroidal separation derived from comparison with fast camera data from MAST. Measurements of the toroidal separation of the filaments from camera images indicate the toroidal separation of the filaments have a double exponential distribution [20], suggesting the lack of a toroidal mode structure. This extended framework is in good agreement with radial profiles of the average D_α emission from the outer mid-plane and its variance. It indicates that the toroidal velocity does not affect the shape of time-averaged profiles in axisymmetric systems.
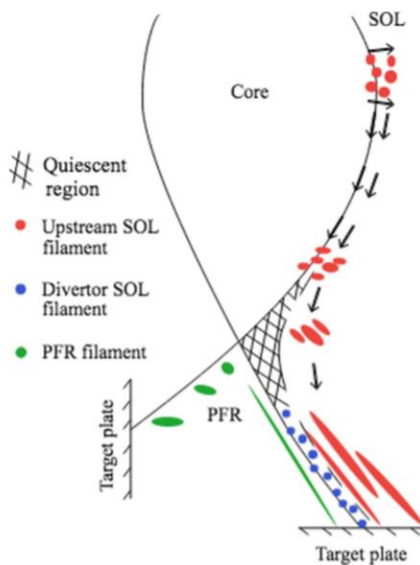

Figure 4: Schematic of the different contributions to intermittent cross-field transport in the divertor observed in MAST. Reproduced from [21].

Understanding transport in the divertor region is challenging in experiments due to the paucity of data and diagnostic access and in simulations due to the high magnetic shear in the vicinity of the X-point and the wide range of transport, atomic, molecular and other processes at work. High-speed imaging of the lower divertor in MAST indicates the presence of several regions where the characteristics of the observed filaments are qualitatively different, including the far SOL of the outer leg due to filaments generated upstream and sheared by the X-point, small (~1cm) high frequency filaments close to the separatrix of the outer leg away from the X-point and in the private flux region [21], as illustrated in Figure 4. A quiescent region devoid of filaments has been recently identified in the outer divertor leg in the vicinity of the X-point [22], with a radial extent spanning from the separatrix to ψ_n ~ 1.02, approximately 1 e-folding length of the heat flux profile from the separatrix, containing around 60% of the heat deposited to the divertor. This quiescent region has been observed over a broad range of operating conditions in L and H-mode, over a wide range of electron density and auxiliary heating power.

BOUT++ simulations of turbulent transport in a simplified sheared slab geometry were carried out to identify the dominant sources of heat and particle flux spreading in a divertor leg. In these simulations, the dominant transport mechanism is due to the Kelvin-Helmholtz instability, driven by radial variations in the electron temperature at the target, and hence the electrostatic potential at the

sheath edge. This leads to the production of large structures which transport heat and particles from the scrape-off layer into the private flux region, whereas the interchange mechanism predominantly acts non-linearly on existing structures. The angle between the divertor leg on the curvature vector strongly influences transport into the private flux region via the interchange mechanism, promoting transport in inner divertor legs where the curvature is directed toward the private flux region, and against transport in typical outer legs. This will motivate future modelling efforts and experiments in long-leg divertors in MAST Upgrade to understand the influence of divertor geometry on heat and particle transport. An empirical scaling of the width of the divertor heat flux footprint mapped to the outer mid-plane, λ_q, has been derived from a database of IR imaging data of L-mode pulses [23]. Impurity transport in the scrape-off layer was studied using coherence imaging that captures the radial and vertical variation of the flows of impurity ions along magnetic field lines. Imaging of C^{2+} flows on the high field-side in the early phase of MAST discharges where the plasma was limited on the centre column revealed counter-streaming impurity flows when high-field side gas fuelling was applied [24]. These flow patterns have been reproduced in EMC3-EIRENE simulations, which indicate that they are driven by enhanced pressure on field lines where the gas is ionised.

The steady-state divertor loads can be mitigated by using detachment to dissipate the plasma heat flux, however deep detachment can lead to strong radiation at the X-point and reduced core confinement. MAST-U will have unprecedented flexibility to tailor the magnetic geometry within up-down symmetric, tightly baffled divertor chambers and excellent diagnostics to improve our understanding of detachment onset and control with a radiating zone in the leg away from the X-point in conventional and alternative divertor configurations, such as the Super-X [1]. The sensitivity of detachment to external control was studied using an analytic 1D model along the magnetic field [25] including heat conduction and impurity concentration to estimate the 'detachment window', i.e. the variation of the upstream density, power crossing the separatrix (P_{SOL}) and radiation from
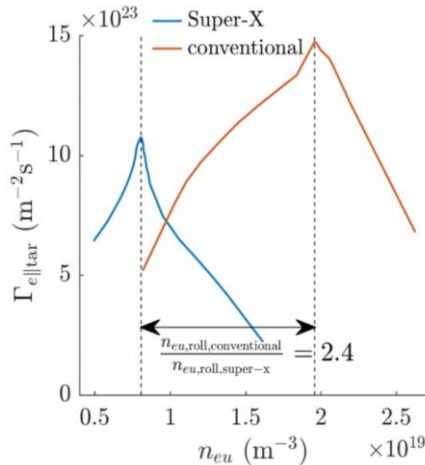

Figure 5: Roll over of the divertor target particle flux with upstream density in conventional and Super-X configurations.

impurities that leads to the detachment front moving from the divertor target to the X-point. It was found that, for a given divertor configuration, the detachment window is greatest for variations in the impurity concentration, followed by P_{SOL} then upstream density. The detachment window for all parameters increases with the ratio of the total magnetic field at the X-point and the divertor target. In spherical tokamaks such as MAST-U where the magnetic field drops significantly with major radius, this ratio can be higher than in a typical divertor in a conventional aspect ratio device (around 3 and 1.3 respectively) if the leg is moved to large major radius, suggesting a wider operational space with detached divertors and improved real-time control of the location of the detachment front. The impact of increasing the major radius of the divertor leg was studied using SOLPS-ITER simulations in a minimally complex slot divertor geometry [26], finding that electron density increases and temperature decreases with increasing major radius, according $f_R^2 = B_u^2/B_t^2$, the total magnetic field upstream and at the divertor target respectively. The roll-over of the divertor particle flux with increasing density, emblematic of the onset of detachment, is found to occur when Te at the divertor target reaches ~0.6eV, independent of the strike point major radius, but the upstream density required to reach this threshold halves when f_R is doubled, suggesting the Super-X should reach detachment at much lower upstream density compared with a conventional configuration. These findings were confirmed in simulations in a realistic MAST-U geometry [27] where the upstream density is increased, shown in Figure 5, in divertor configurations where the strike point major radius in the Super-X is twice that of the conventional. This leads to a factor 2.4 reduction in the upstream density required to reach detachment for otherwise similar operating parameters. In simulations of the Super-X configuration where nitrogen impurity seeding into the divertor is used to reach detachment, the region of greatest radiation emission moves toward the entrance to the baffled divertor at the highest seeding rates, thereby avoiding possible core confinement degradation associated with strong radiation at the X-point. In these SOLPS-ITER simulations, collisions between plasma ions and molecules is identified as an important sink of momentum at and beyond the detachment threshold. Deeper insights into the fundamental processes governing

the onset and evolution of detachment have been provided by 1D simulations carried out using the BOUT++ module SD1D [28]. For MAST Upgrade-like parameters, power dissipation through radiation is required for detachment to occur, and the energy required to ionise neutrals is required to vary with T_e, either through hydrogenic or impurity radiation, is needed to reduce the target particle flux. Volume recombination is not expected to play a major role except in full detachment.

6. PREPARATIONS FOR MAST UPGRADE OPERATIONS

MAST Upgrade is currently transitioning to operations, following a successful construction phase (the completed interior is shown in Figure 6). The vacuum vessel and its interior components have been baked to achieve good vacuum conditions. Activities carried out in preparation for the plasma operations have concentrated on ensuring the operating space is as wide as possible and the novel implementation of diagnostics to enable detailed physics studies. The minimum density and highest β achievable in tokamaks can be determined by the amplitude and spectrum of 3D error fields introduced by imperfections in the manufacture and/or alignment of the poloidal field coils. A rigorous characterisation of the intrinsic error field has been carried out through high precision 3D measurements of the magnetic field produced by the poloidal field coils in the main chamber and divertors that indicate the dominant harmonics have toroidal mode numbers n = 1, 2. These measurements were used to determine the optimum orientation of each coil to minimise the n = 1 harmonic, which as then applied during the final alignment of the coils. Active compensation of the residual n = 1 and n = 2 error fields will be carried out using a combination of ex-vessel and in-vessel coils respectively, guided by modelling using the ERGOS vacuum model and MARS-F linear single fluid MHD code to optimise the active control of the n = 2 harmonic.

Figure 6: Photograph of the completed interior of MAST Upgrade prior to being pumped down.

The first experimental campaign is expected to commence in 2019, utilising the new capabilities provided by the upgrade and high-resolution diagnostics to address key physics issues for the operation of ITER and the design of DEMO, principally plasma exhaust, energetic particle physics and the development of integrated scenarios. Novel electrical modules utilising field programmable gate arrays will operate the real-time protection system, divertor Langmuir probes [29] and foil bolometer arrays [30] will provide unprecedented flexibility and data quality. Data analysis and comparison with modelling will be significantly improved using the new CHERAB and Raysect tools [31, 32]. A phased programme of enhancements is underway to address key gaps in the EUROfusion plasma exhaust strategy for finding a solution to the heat exhaust in a reactor, involving 5MW of additional NBI heating, a cryoplant to serve the existing cryopumps, a high frequency pellet injector and new and upgraded diagnostics including new fast imaging cameras viewing the main chamber SOL and IR cameras, infrared video bolometers and a Thomson scattering system viewing the X-point [33].

ACKNOWLEDGEMENTS

REFERENCES

[1] A. W. Morris et al., IEEE Trans. Plasma Sci. **46** 5 1217-1226 (2018)

[2] M. Valovič et al., Nucl. Fusion 51 073045 (2011)

[3] S. Kaye et al., Nucl. Fusion **47** 499 (2007)

[4] G. J. Colyer et al., Plasma Phys. Control. Fusion **59** 055002 (2017)

[5] M. F. J. Fox et al., Plasma Phys. Control. Fusion **59** 044008 (2017)

[6] M. F. J. Fox et al., Plasma Phys. Control. Fusion **59** 034002 (2017)

[7] F. van Wyk et al., Plasma Phys. Control. Fusion **59** 114003 (2017)

[8] M. Cecconello, A. Sperduti, Plasma Phys. Control. Fusion **60** 055008 (2018)

[9] B. Madsen et al., Rev. Sci. Instrum., in press "Velocity-space tomography using prior information at MAST"

[10] M. Cecconello et al., subm. Nucl. Fusion "Discrepancy between estimated and measured fusion product rates on MAST using guiding-centre approximation"

[11] K. G. McClements et al Plasma Phys. Control. Fusion **60** 095005 (2018)

[12] K. G. McClements et al Plasma Phys. Control. Fusion **60** 025013 (2018)

[13] J.F. Rivero-Rodriguez et al, Rev. Sci. Instrum., in press "A rotary and reciprocating scintillator based fast-ion loss detector for the MAST-U tokamak"

[14] B. Hnat et al Plasma Phys. Control. Fusion **60** 085016 (2018)

[15] S. Murphy-Sugrue et al., Plasma Phys. Control. Fusion **59** 055007 (2017)

[16] N. R. Walkden et al., Rev. Sci. Instrum. **86** 023510 (2015)

[17] K. Flesch et al., "Effect of RMP application on neutral fueling and exhaust in MAST", Plasma-Surface Interactions in Controlled Fusion Devices conference (2018)

[18] F. Militello et al., Plasma Phys. Control. Fusion **59** 125013 (2017)

[19] F. Militello et al., Phys. Plasmas **25** 056112 (2018)

[20] T. Farley et al., Proc 45th EPS Conf. 2018

[21] J. R. Harrison et al., Phys. Plasmas **22** 092508 (2015)

[22] N. R. Walkden et al., Nucl. Fusion **57** 126028 (2017)

[23] S. Elmore et al., Proc 45th EPS Conf. 2018

[24] I. Waters et al., Nucl. Fusion **58** 066002 (2018)

[25] B. Lipschultz, F. I. Parra, I. H. Hutchinson, Nucl. Fusion **56** 056007 (2016)

[26] D. Moulton et al., Plasma Phys. Control. Fusion **59** 065011 (2017)

[27] D. Moulton et al., Proc 44th EPS Conf. 2017

[28] B. D. Dudson et al., subm. NME "The role of particle, energy and momentum losses in 1D simulations of detachment" (2018)

[29] J. Lovell et al., JINST **12** C11008 (2017)

[30] J. Lovell et al., Rev. Sci. Instrum. **87** 11E721 (2016)

[31] M. Carr et al., Proc 44th EPS Conf. 2017

[32] M. Carr et al., Rev. Sci. Instrum., in press "Description of complex viewing geometries of fusion tomography diagnostics by ray-tracing" (2018)

[33] J. R. Harrison et al., Proc 43rd EPS Conf. 2016